

Fabrication of a Ceramic Foam Catalyst Using Polymer Foam Scrap via the Replica Technique for Dry Reforming

Rungsima Yeetsorn,* Sabaithip Tungkamani, and Yaowaret Maiket

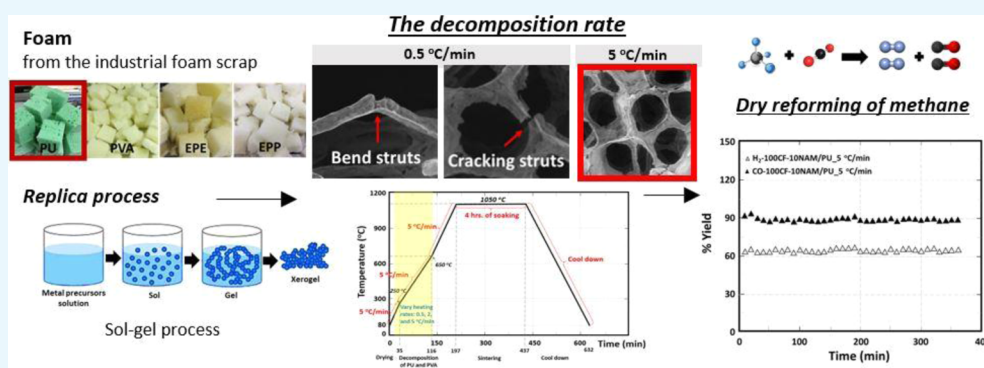
Cite This: *ACS Omega* 2022, 7, 4202–4213

Read Online

ACCESS |

Metrics & More

Article Recommendations



ABSTRACT: Megapores with spherical-like cells connected through windows and high porosities make up catalyst supports in the form of ceramic foams. These characteristics provide significant benefits for catalytic processes that are limited by mass or heat transport. This study focuses on the manufacture of ceramic foam using a polymeric sponge replica process and polymer foams as a template for catalyst supports, which are industrial waste from the packaging sector. To make ceramic foam catalysts, they were dipped in a catalyst solution, followed by a breakdown stage and a sintering process. Experiments focused on determinants that affect the desired characteristics of ceramic foams, such as the types of polymer foams that affect foam morphology, the rheology of catalyst solution that affects catalyst dispersion, and the polymer decomposition rate that affects catalytic performance during dry reforming of the methane process. The cell architectures of polyurethane and polyvinyl alcohol foams are attractive for catalyst support preparation because they have 98–99% porosity and typical cell sizes of 200 and 50 μm , respectively. The polyurethane performance was superior to the performance of polyvinyl alcohol in terms of higher porosity and better catalytic-solution absorption offering high catalyst active areas. The catalyst prepared from concentrated 10 wt % Ni/Al₂O₃–MgO (10NAM) slurry had the highest surface area (59.18 m²/g) and the highest metal oxide dispersion (5.65%). These results are relevant to the flow behavior of catalyst slurry which plays a key role in coating the catalyst gel on the polymer template. The thermal decomposition rate used to remove the polymer template from the catalyst structure is proportional to the ceramic foam structure (catalyst support structure). The slow decomposition rate bent and fractured foam-cell struts more than the faster rate. On the other hand, achieving good catalyst dispersion on catalyst supports necessitated a high sintering rate. When sintering was adjusted at a high sintering rate, the metal–particle dispersion was relatively high, around 7.44%, and the surface area of ceramic foam catalysts was 64.61 m²/g. Finally, the catalytic behavior toward hydrogen production through the dry reforming of methane using a fixed-bed reactor was evaluated under certain operating conditions.

INTRODUCTION

Unlike most industries during the COVID-19 outbreak, plastic manufacturers saw production increase in the midst of a global economic downturn, especially plastic packaging demand for logistics and delivery related to e-commerce sales. These situational sudden changes resulted in around 12% increase in industrial scrap and domestic waste generation,^{1,2} thus adequate waste management procedures are required. Polymer foams³ are the most versatile plastics used for logistics and delivery processes. They are an interesting material to be applied as a template for ceramic foam production due to their cellular

structure. Ceramic foams are produced as positive images of synchronous polymer foam structures and show bed porosities as high as 85–90% that make them interesting as catalyst

Received: October 18, 2021

Accepted: January 18, 2022

Published: January 27, 2022



supports compared to conventional heterogeneous catalysts. Ceramic foams typically retain a large number of pores and a high geometric surface area, good thermal properties, high strength, and resistance to chemical attacks.^{4–8} In a reactor containing ceramic foam cartridges rather than packed particles, the high bed porosity allows for a low pressure drop, increased turbulence, and improved heat transfer and mass transmission. Furthermore, the interconnectedness of the ideal pore structure of typical catalysts should be high. High convection in the tortuous megapores improves mass and heat transport,⁹ whereas the degree of interconnectivity corresponds to a decrease in pressure drop. Highly endothermic and exothermic reactions in long, thin reactor tubes, as well as selective partial oxidation with short contact durations, require these advantages.¹⁰ The characteristics of ceramic foams are similar to those of monolithic structures containing thousands of parallel channels defined by many thin walls in a honeycomb structure.¹¹ High-flow resistance and back pressure will arise within the system if undesired mass transfer and heat transfer happen in a catalyst structure due to its limited surface area and porosity, resulting in increased power loss and less retention time of reactants on catalyst surfaces. Many industrial catalysts, such as pellets, are frequently used in heat transfer-limited conditions. To provide the requisite heat transfer surfaces, many long reactor tubes with a small diameter are often used to assist heat transfer in the process. The use of lengthy, narrow tubes may result in a significant pressure drop penalty.¹² Creating larger catalyst pellets is a strategy to reduce the pressure drop; however, this situation may cause an increase in radial heat transfer, a decrease in efficiency, and a requirement of more catalyst volume. To relieve all these problems, fabricating ceramic foams in the form of cylindrical cartridges precisely inside the reactor tube is one of the good solutions. The ceramic foam can be produced using various methods, such as, the polymeric sponge replica method, the direct foaming method, and the pore-forming method.¹³ The replica sponge technique is the most conventional procedure to create ceramic cellular structures because the ceramic structure is stabilized and failure of smaller pores can be prevented.^{14–16} Prior to the polymeric sponge replica process, a catalyst solution was prepared via the sol–gel process, involving conversion of monomers into a colloidal solution (sol) that acts as the precursor for an integrated network (or gel) of discrete particles.¹⁷ For the design of catalytic formulations based on metals and metal oxides with a high degree of structural and compositional uniformity, the sol–gel method is used. The hydrolysis and condensation of metal alkoxides gave rise to this process, and the sol–gel chemistry has a plethora of techniques for producing catalysts from solution state precursors. Low-temperature chemistry, repeatability, and high surface-to-volume ratios of produced products are some of the remarkable features of this fascinating technique for modifying the physicochemical properties of catalysts.¹⁸ The replication of a polymeric template includes the immersion of a polymeric sponge in a ceramic or metallic suspension with a solid content.¹⁹ Next, the impregnated polymer template is transposed from the slurry, and the excess slurry is squeezed out. The polymer template and organic substances will be burnt out via drying and thermal treatment processes, and then ceramic skeletons will be obtained after ceramic particles are sintered at a high temperature. The shrinkage of ceramic catalyst supports linked to the thermal treatment and sintering steps is carefully considered to obtain ceramic skeletons structured like a template.²⁰ Ceramic foams have typically been applied to

several industrial catalytic processes, namely, methane reforming, Fischer–Tropsch synthesis, carbon dioxide methanation, ethylene epoxidation, and catalytic combustion.²¹ Since most hydrogen can be generated through methane reforming, a high-temperature process in which steam combines with a hydrocarbon fuel to produce hydrogen, this work focuses on methane reforming to produce hydrogen for additional hydrogen energy applications. Hydrogen energy is a type of energy that has high energy efficiency, a wide range of environmental and social benefits, and is economically competitive. It is a viable transportation and power generation fuel that may be utilized in automobiles, portable power supplies, and stationary applications. Additionally, an increase in hydrogen demand as a feedstock for various processes can be continuously found. This work is interested in developing ceramic foam for dry reforming of methane (DRM), attractive from an environmental point of view because it consumes two major greenhouse gases (CH₄ and CO₂). DRM is a hydrogen production process that converts greenhouse gases (methane and carbon dioxide) to synthesized gas or syngas (carbon monoxide and hydrogen).

Even though ceramic foam generation has been documented throughout literature, there have been few systematic studies of the idea of repurposing industrial waste to generate clean energy that can be utilized as a precursor for fuel cell, petrochemical, or chemical processes. A regenerative strategy toward replacing the traditional linear economy is to create a circularity to eliminate waste and ensure the continued use of resources. Detailed research on the selection of polymer foam for use as a catalyst template and the manufacture of a nickel-alumina magnesium catalyst utilizing the reticulated sponge technique and a polymeric template is presented in this paper. In addition, the viability of using newly developed catalysts was assessed by observing their potential throughout the DRM reaction. To develop ceramic foams with the same structure as the employed polymeric foam template, researchers looked into catalyst suspension viscosity, polymer foam absorption ability, active metal dispersion, and thermal treatment and sintering process parameters.

RESULTS AND DISCUSSION

Polymer Foam Selection for Applying as a Catalyst Template. Cell characteristics play an imperative role in transport phenomena and foam properties; especially regarding elasticity, permeability, and fluid absorption.²² The microstructures of polymer foam scraps, polyurethane (PU), polyvinyl alcohol (PVA), expanded polyethylene (EPE), and expanded polypropylene (EPP) foams, supplied by furniture and packaging factories are given in Figure 1. The polymer foams have interconnectivity between both solid faces (closed-cell structure) and open interconnecting faces (open-cell structure). Closed cells critically absorb slurry, while the slurry effortlessly transfers into the foam pores containing interconnecting open cells. Therefore, EPE and EPP owned relatively closed cells that are not suitable for the ceramic foam preparation. Considering the open interconnecting porosity of polymer cells analyzed using a gas pycnometer, it was found that PU and PVA possessed the highest porosities, which varied from 98 to 99%, followed by 69 and 43% of the porosities of EPP and EPE, respectively. Consequently, PU and PVA were handpicked for further exploration. The cell size, strut size, and cell density of polymer foams were observed from optical microscope (OM) images and calculated using SemAfore 5.2.1 software; these values are presented in Table 1. The results indicated that both PU and

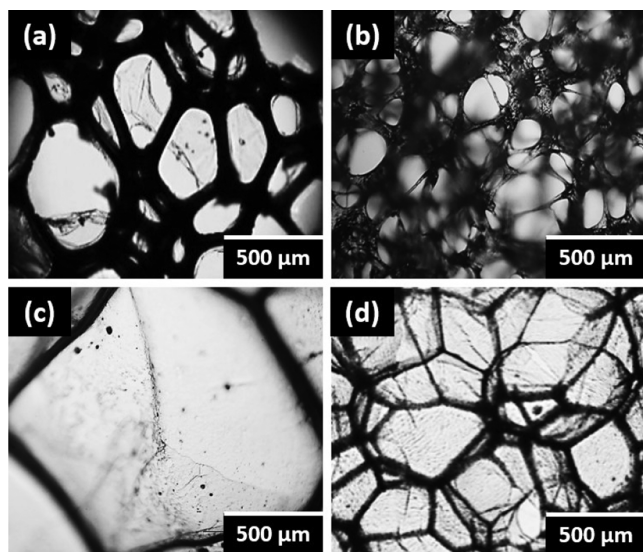


Figure 1. Optical microscopic images (magnified 5 \times) of polymeric foams PU (a), PVA (b), EPE (c), and EPP (d).

Table 1. Cell Size, Strut Size, and Cell Density of PU and PVA Foams

polymeric foam	cell size (μm)	strut size (μm)	cell density (no. of cell/ $1.89 \times 10^6 \mu\text{m}^2$)
PU	220.40	50.70	11
PVA	68.50	25.29	283

PVA have comparable porosity values, but the average cell size of PVA is significantly smaller than that of PU. A smaller pore size brings about smaller transport of fluid permeation and higher flow resistance of slurry.²³ Furthermore, a large strut size may be realized with sufficient strength of ceramic foam products.²⁴

Figure 2 illustrates the morphology of polymer foams structured with three components: (1) struts which act as a

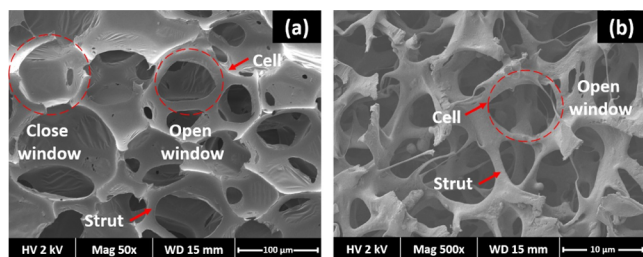


Figure 2. SEM micrographs of PU (a) and PVA foams (b).

structural support for the foam, (2) cells which are voids enclosed by struts, and (3) windows which are open/closed, interconnecting cells to each other.²¹

The removal of the polymer foam template by calcination is a key stage in the manufacturing of foam ceramics; hence, the decomposition temperature of the polymer foam template is required for optimizing an operating condition. The thermal behavior of polymeric foam was analyzed using the thermogravimetric analyzer (TGA) under air flow and temperature sweep from 30 to 800 $^{\circ}\text{C}$ with the heating rate at 5 $^{\circ}\text{C}/\text{min}$; the results are presented in Figure 3. The urethane bonds of the PU foam initially degrade at a decomposition temperature of 228 $^{\circ}\text{C}$, and then isocyanate gas is generated with a 28.36% weight loss.^{25–27} At the temperature of 331 $^{\circ}\text{C}$, which is the second

transition, the decomposition of monomers and polyol molecules was completed with a 65.01% weight loss. In terms of the PVA foam, the preliminary degradation occurred at approximately 50 $^{\circ}\text{C}$ when small molecules were produced. Hydroxyl groups and polymer chains were decomposed at 320 $^{\circ}\text{C}$ of the decomposition temperature. The main decomposition happens at 390 $^{\circ}\text{C}$ where carbon oxide molecules and volatile hydrocarbons decompose.^{28–31} According to the analyzed results of the polymer foam characteristics, PU and PVA foams were chosen to be catalyst templates. The catalyst slurry of 10NAM was prepared as described in the experimental section, and the temperature profile as a function of time for eliminating a polymer template and sintering was composed as shown in Figure 4. To make sure that the polymer template was completely removed, the temperature range applied to the template elimination step was 250–650 $^{\circ}\text{C}$ with a 5 $^{\circ}\text{C}/\text{min}$ heating rate related to decomposition temperatures of PU and PVA foams. The discussion about overall heating steps for ceramic foam fabrication will be stated in the further section, “effect of thermal treatment on the ceramic foam structure”. Prepared ceramic foam features were preliminarily investigated through scanning electron microscopy (SEM) images (Figure 5). CF-10NAM/PU exhibited open cells consisting of uniform open interconnecting pores, while CF-10NAM/PVA showed a rather non-uniform structure and a smaller number of open cells than those of CF-10NAM/PU. The CF-10NAM/PU structure looks quite similar to the original polymer foam template, and its features are comparable to those of a conventional ceramic foam.³² The undesirable morphology of CF-10NAM/PVA was due to the 10NAM slurry not impregnated into the cell and the solid particles in the slurry agglomerated on the surfaces of the foam template. This configuration leads to poor heat and mass transfer.

Nitrogen physisorption was used to establish the isotherms of adsorption, the distribution of pore size, pore geometry, connectivity, and the specific surface area.³³ These values theoretically play a crucial role in determining the diffusion and transport of molecules in the heterogeneous catalytic reaction. Adsorption hysteresis (Figure 6) is a correlation between the shape of the hysteresis loop and the textures of a mesoporous (pore sizes between 2.0 and 50.0 nm) material. Similar adsorption–desorption isotherms were investigated with explicit hysteresis loops at a slightly lower relative pressure (P/P_0) for CF-10NAM/PVA and CF-10NAM/PU in comparison to the supports. The catalysts occupied normal porous networks of isotherms type V with narrow H3-type hysteresis loops with regard to hysteresis loop types categorized by IUPAC.^{34,35}

The H3 hysteresis is attributed to slit-shaped pores, and the isotherms do not indicate any limiting adsorption at high P/P_0 . The isotherms are observed with non-rigid aggregates of plate-like particles.³⁶ The ceramic catalyst using PU foam as the template shows a nano-pore size (12.96), pore volume (0.19 cm^3/g), and high surface area (59.18 m^2/g), as shown in Table 2. These values can be interpreted that the PU foam, having more open cells and a larger cell size than those values of the PVA foam, was able to adsorb gas more than the PVA foam. Moreover, it provided a higher surface area than that of the PVA foam. According to the consideration of cell morphology, the isotherms of adsorption, and the surface area of catalysts, the PU foam template was selected for the catalytic performance test.

To set up the testing set for the subsequent catalytic performance test, catalyst reducibility was assessed using

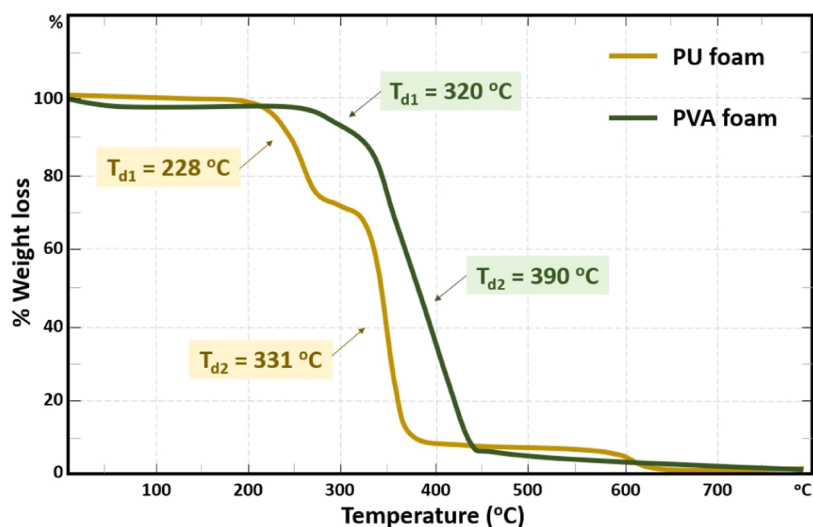


Figure 3. Thermogravimetric curves of PU and PVA foams.

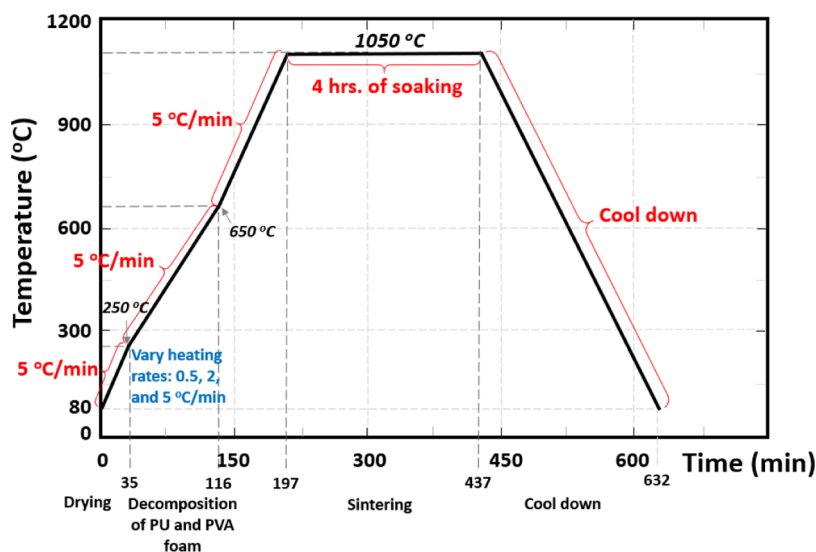


Figure 4. Thermal treatment profile for the ceramic foam catalyst.

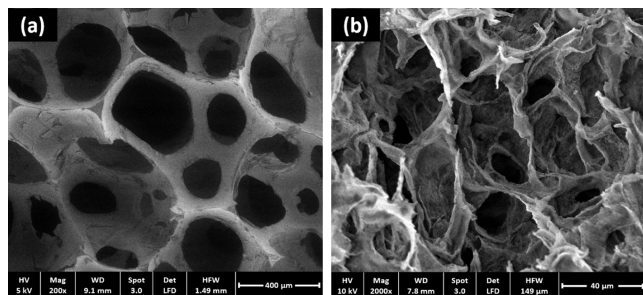


Figure 5. SEM images of prepared ceramic foams: CF-10NAM/PU (a) and CF-10NAM/PVA (b).

temperature-programmed reduction (TPR). TPR is a technique that is extensively used in catalysis research to investigate the surface chemistry of metals and metal oxides at various thermal settings. TPR collects quantitative and qualitative data on reducing gas mixes that are used to flow over metal oxide samples.³⁷ It offers accurate insights into catalyst reducibility and reaction rates in the presence of metal surfaces. The reduction profiles (Figure 7) illustrate two main areas of interest

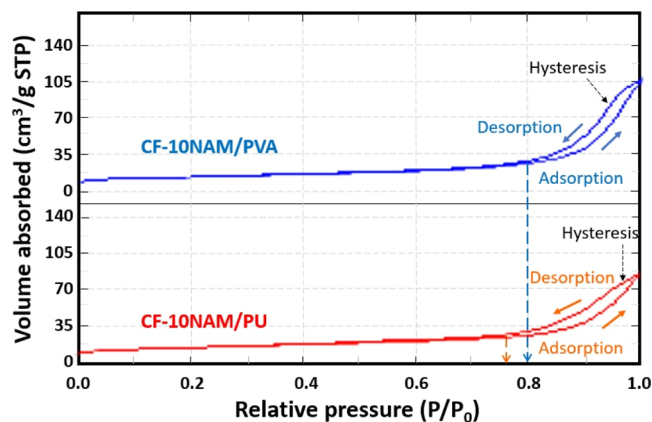
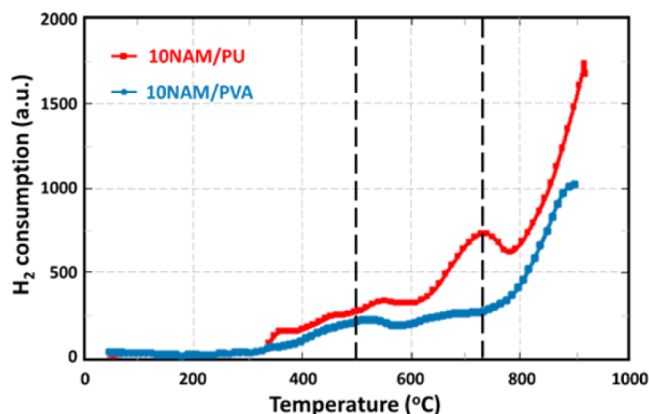


Figure 6. N₂ adsorption–desorption isotherm of 10NAM ceramic foam catalysts.

in which many H₂-consumption peaks can be detected. The first series of peaks occur at temperatures between 400 and 600 °C. The second part indicates that the H₂ consumption appears at higher temperatures from 600 to 780 °C.

Table 2. BET-Surface Area, Pore Volume, and Pore Size of the Ceramic Foam Catalyst

ceramic foam catalyst	surface area (m ² /g)	pore volume (cm ³ /g)	average pore size (nm)
CF-10NAM/PU	59.18	0.19	12.96
CF-10NAM/PVA	48.68	0.24	19.83

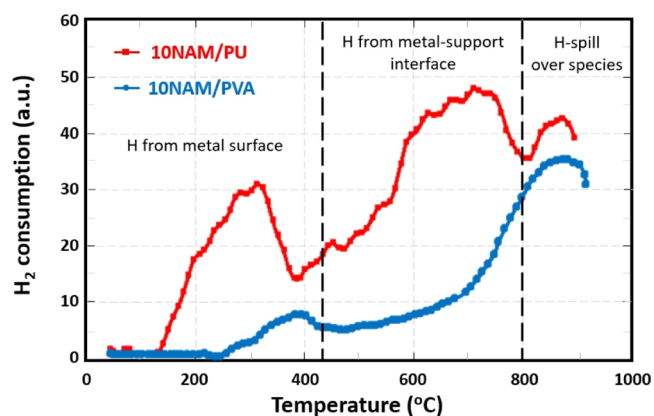
**Figure 7.** H₂-TPR of 10NAM ceramic foam catalysts fabricated from polymer foam templates.

The temperature-programmed reduction of hydrogen (H₂-TPR) profiles typical of catalysts containing Ni usually presents two main H₂-consumption peaks.³⁸ The first peak is typically detected at lower-intermediate temperatures that are associated with bulk NiO_x species.³⁸ It is interpreted that the outer layer of Ni²⁺ in the NiO phase was oxidized as a surface reduction.³⁹ The second peak found at higher temperatures is relevant to the reduction of excellently dispersed NiO_x and/or Ni species in good interaction with the catalyst support.³⁸ This peak can be related to the reduction of the inner Ni²⁺ layer (bulk reduction) in Ni_{1-x}Mg_xO and Ni_{1-y}Mg_yAl₂O₄ phases.^{40,41} The results in Figure 7 show that the overall H₂-consumption of CF-10NAM/PVA was significantly lower than that of CF-10NAM/PU. It implies that the reduction performance of CF-10NAM/PVA was inferior to the performance of CF-10NAM/PU. It is worth noting that the obvious H₂ consumption peak at a high temperature for 10-NAM/PVA cannot be detected; the catalyst support formed by the PVA foam did not achieve the desired interaction with catalyst particles.

TPD allows scientists to study the interaction of reaction gases with solid surfaces, thereby being a powerful tool for both the evaluation of active sites on catalyst surfaces and the understanding of the mechanisms of catalytic reactions including adsorption, surface reaction, and desorption. Regarding an assumption for this diagnosis, the number of surface Ni sites per unit mass of the catalyst can be found by means of H₂-TPD, supposing the adsorption stoichiometry ratio of H/Ni is equal to 1:1. The dispersion of Ni can further be calculated based on the volume of chemisorbed H₂,⁴² however; the peak area of the H₂-TPD profile should be normalized by that of H₂-TPR of a standard CuO sample to obtain the actual catalyst dispersion percentage.⁴³ Concisely, the H₂-TPD technique can be applied to study the distribution and dispersion of active metals on the catalyst support. A good catalyst dispersion is expected to provide better reforming efficiency as the dispersion of the metal increases the reaction surface area easily.⁴⁴

In this work, the chemisorption studies provide an overview of the overall adsorption capacities of the catalysts⁴⁴ and the

interaction of H₂ with supported Ni catalysts.⁴⁵ The H₂-TPD profiles of 10NAM ceramic foam catalysts (Figure 8) were

**Figure 8.** H₂-TPD of 10NAM ceramic foam catalysts produced from polymer foam templates.

investigated from three temperature ranges. The temperature at which H species are released helps to comprehend the nature of these species. The H₂-desorption at a temperature below 420 °C is ascribed to the adsorbed H₂ on metal Ni sites, whereas the H₂ desorption between 420 and 800 °C accounts for the H₂ from the metal–support interface.⁴⁶ The desorption at higher temperatures is typically attributed to the H₂ spillover hydrogen adsorbed on the surface of the oxide.^{47,48} The H₂-TPD peak of 10-NAM/PVA cannot be found in the temperature range of 420–800 °C, since the catalyst support did not interact well with the metal catalyst. This particular reason is supported by the dispersion of active metals on the 10NAM/PU and 10NAM/PVA ceramic foam catalysts. The dispersion of active metals on the 10NAM/PU and 10NAM/PVA ceramic foam catalysts is 5.65 and 1.43%, respectively. Ni loading and dispersion typically influence the % conversion of the DRM reaction. The % conversion increases with the growth of metal content due to good catalytic activity. Nevertheless, undesired metal dispersion may occur if the Ni loading is higher than 15%.⁴⁹ This is due to metal sintering, which is created at high Ni content, and the metal sintering leads to carbon formation. Therefore, it is necessary to optimize the Ni loading to achieve good catalytic activity. The Ni loading (10 wt %) was determined from the previous work of our research group, as described in the section “catalytic performance test.”

Based on the current findings, PU foam’s performance as a catalyst template is superior to that of PVA foam because it has a higher porosity and greater ability to absorb catalytic solutions than PVA foam. When comparing the properties of catalysts made with different polymer templates, the PU template produced a catalyst with a greater surface area and better catalyst dispersion on the catalyst support.

Rheological Measurements of Aqueous Oxide Slurry.

The rheological measurements of slurry play a key role in the coating of polymeric foam in the replica technique.^{50–53} In general, the solid content affects the rheology of ceramic slurry and the final structure of the ceramic foam;⁵⁴ therefore, the viscosity values of the ceramic slurry prepared through the sol–gel process with different concentrations were measured.

The viscosity results in Table 3 agree with the typical reason to decrease the flow resistance of catalyst slurry by water dilution. 100CF-10NAM/PU or CF-10NAM/PU occupied the highest

Table 3. Properties of the Ceramic Foam Catalyst with Different Water Dilution

ceramic foam catalyst	slurry viscosity (cP)	surface area (m ² /g)	pore volume (cm ³ /g)	average pore size (nm)	metal oxide dispersion (%)
100CF-10NAM/PU (CF-10NAM/PU)	44.83	59.18	0.19	12.96	5.65
75CF-10NAM/PU	32.37	44.96	0.21	21.17	4.66
50CF-10NAM/PU	9.21	44.96	0.19	16.80	2.98
25CF-10NAM/PU	0.94	33.47	0.17	19.36	2.90

surface area (59.18 m²/g), while the surface area (33.47 m²/g) of 25CF-10NAM/PU was inferior to the others. The 100CF-10NAM slurry had higher apparent viscosity, obviously for suspensions with higher solid concentrations.⁵⁵ There seems to be a particular reason to ascribe transport rationality; high viscosity allowed catalyst solids to be efficiently carried into pores of a foam template. This phenomenon corresponds to high relative density and low foaming capacity resulting in a smaller average pore size.⁵⁴ Even though the slurry viscosity is important for the ceramic coating process, metal dispersion was parallelly concerned in terms of the reactivity, which directly impacts catalyst performance.

TPR of ceramic foam catalysts with various concentrations under H₂ flow gas is shown in Table 4. Peaks of all samples were

Table 4. H₂ Consumption was Observed via H₂-TPR of Ceramic Foam Catalysts

samples	1st peak temperature (°C)	2nd peak temperature (°C)	H ₂ consumption (a.u.)
25CF-10NAM/PU	440	675	266.64
50CF-10NAM/PU	450	680	433.14
75CF-10NAM/PU	485	709	614.90
100CF-10NAM/PU	550	714	728.18

evidently perceived in the temperature range of 400–600 °C, relating to the reduction of Ni oxide aggregates. The second broad peak appeared around 700 °C, corresponding to the reduction of the Ni species that strongly interacted with the Mg(Al)O support.^{56–58}

The metal dispersion of the ceramic foam catalyst with different water contents was monitored via H₂-TPD analysis, as shown in Figure 8. Areas under the peaks of TPD profiles illustrate that the efficiency of metal dispersion on the catalyst support decreased with a decrease in viscosity, from 44.83 to 0.94 cP. The 100CF-10NAM/PU with the highest viscosity generated a uniform ceramic foam structure and good dispersion of solid particles. It is worth mentioning that the low-viscous slurry brought about better solid distribution than the one with higher viscosity did. The active metals will be able to distribute throughout the surface area of a polymer foam template.⁵⁹ It is difficult to achieve a good dispersion; plenty of slurries deposited on the bottom portion of the sponge are regularly found.⁶⁰ A dense microstructure may develop as a result of the failure of impregnation of high-viscous slurry into the foam template, and it stays on its surface. The TPD behavior of hydrogen on the ceramic foam catalysts was studied via the reduction process in order to obtain information on the Ni surface area and dispersion.⁶¹ The hydrogen consumption peak can be separated into two temperature ranges which are 120–400 and 400–900 °C (Table 5).

The low temperature is typically attributed to the physical adsorption of H₂ weakly adsorbed on the metal surface, and it indicates the exposed fraction of Ni atoms. The high temperature is originated from chemisorbed H₂ in the

Table 5. Dispersibility Observed via H₂-TPD of Ceramic Foam Catalysts

samples	1st peak temperature (°C)	2nd peak temperature (°C)	dispersion (%)
25CF-10NAM/PU	300	750	2.80
50CF-10NAM/PU	350	820	2.98
75CF-10NAM/PU	300	800	4.66
100CF-10NAM/PU	330	740	5.65

subsurface layers and from spillover H₂.^{61,62} The data provides compelling evidence, 5.65% of the metal dispersion degree and 51.12 m²/g of the surface area, indicating that the 100CF-10NAM provided superior performance than the others.

Effect of Thermal Treatment on Ceramic Foam Efficiency. To optimize overall porosity and foam microstructure, the sintering temperature should be carefully imposed in addition to the ceramic slurry concentration and operating conditions for the sol–gel reaction. To develop a successful structure with an increase in the mechanical properties of ceramic foams, the sintering schedules must be modified to become thick and strong struts and cell walls.⁶³ The decomposition temperature of polymer foam was used as a benchmark for removing a polymer template from the catalyst support, and an appropriate heating rate to decay the polymer foam had an impact on the microstructures of ceramic foam. As a result, discussion of the influence of various heating rates, 0.5, 2, and 5 °C/min, on the ceramic foam structure and H₂ reduction efficiency has been included in the article. Figure 4 exhibits the thermal treatment program including two major steps: the foam decomposition stage at 250–650 °C and the sintering stage under isothermal conditions at 1050 °C. The heat treatment was first scheduled by heating the resulting catalyst with a heating rate of 5 °C/min from 80–250 °C to remove the residue water, and then the temperature was raised to 650 °C for burn-out PU support. Three different heating rates applied at the stage were investigated, as mentioned above. Subsequently, the sample was heated to 1050 °C at 5 °C/min with 4 h of soaking for sintering of the created ceramic foam. After the thermal cycle was completed, the samples were left in the furnace for cooling down to room temperature. The morphology of the sintered ceramic foams was investigated by SEM, as illustrated in Figure 5. The SEM images present the structure of CF-10NAM/PU observed to be of a typical cellular nature. The cells appear to be nearly spherical in shape and connected to each other. Based on the decomposition temperature of PU foam (Figure 3), an abrupt burn-out of the PU template may generate cracks in the porous framework.¹³ Hence, an optimal heating rate is very much crucial to prevent cracks and other defects.

Based on the theoretical hypothesis, the ceramic catalyst can possibly create a dense structure at a slow heating rate better than forming ceramic foam at a high heating rate. Nevertheless, the bent and failure struts were found when 0.5 °C/min of the heating rate was applied. The particular reason may be associated with degradation of significant portions of the PU sponge. According to TGA results of PU foam, the PU was

degraded by approximately 28% with weight loss at around 228 °C and mainly degraded at roughly 331 °C. PU deterioration was occurring at 0.5 °C/min at those temperatures, with a significant weight loss, but the ceramic particles had not evenly fused into a ceramic foam structure because the microstructure temperature had not yet reached the fusing temperature. As a result, the density and heat conductivity in various sections of the ceramic structure were not homogeneous, resulting in partial stress accumulation in the microstructure. Struts and the plateau border structure tighten as a result of the stress; further shrinking causes strut bending and cracking (Figure 9).

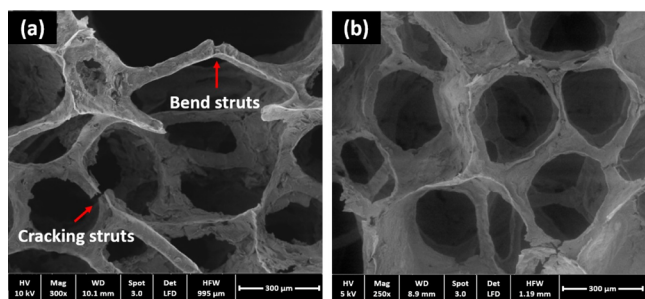


Figure 9. SEM images of ceramic foams with decomposition rates of 0.5 (a) and 5 °C/min (b).

The features of catalysts influenced by the heating rate were investigated by the Brunauer–Emmett–Teller (BET) technique (Table 6). The results showed that the average pore volume of all 100CF-10NAM/PU catalysts was equivalent. In terms of surface area, average pore size, and metal oxide dispersion, the 100CF-10NAM/PU catalyst prepared via 5 °C/min of heating rate indicated the best characteristics among other catalysts in this series (Table 6). In the scenario of a TPR profile, the results of all catalysts presented a main area of interest in which several H₂-consumption peaks can be observed in the temperature range of 500 to 700 °C. It means that the H₂ reduction of finely dispersed NiO_x and/or Ni-species is in tight interaction with the catalyst support.³⁸ The H₂ consumption of the produced 100CF-10NAM/PU catalyst with 5 °C/min of heating rate was obviously predominant compared to the rest of the catalysts (Figure 10). The 100CF-10NAM/PU₅ °C/min used hydrogen for reducing oxides in a wide range of 200–700 °C, and the optimum reducing temperature was found at 620 °C which was the peak of the H₂ consumption curve. The 100CF-10NAM/PU using the heating rate of 0.5 and 2 °C/min showed two reduction intervals. The reducing temperature ranges of 100CF-10NAM/PU_{2.0} °C/min were 300–430 and 430–750 °C, while the suitable temperature for reducing was 650 °C. In the case of 100CF-10NAM/PU_{0.5} °C/min, the reduction intervals were in the range of 300–550 and 550–750 °C and the optimum reducing temperature was 600 °C. According to previous publications related to the reducibility of nickel in the Ni/MA catalyst,^{64–67} three reduction peaks were typically observed in the Ni/MA catalyst. The lowest reduction

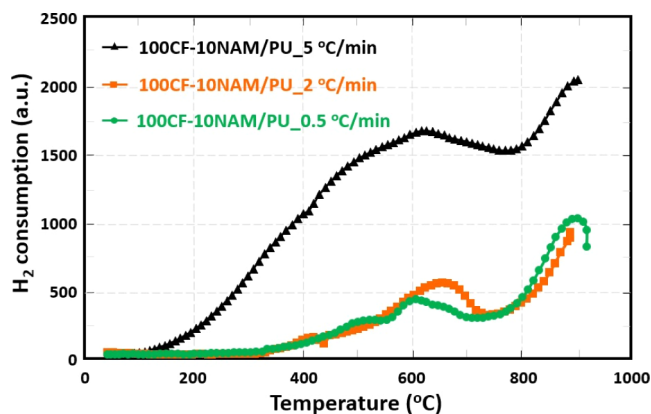


Figure 10. H₂-TPR of ceramic foam catalysts with different decomposition rates.

temperature peak can occur in the range of 150–350 °C, corresponding to the reduction of free NiO or NiO which possesses weak integration between NiO and Al₂O₃ support. The second peak is typically in the temperature range of 370–500 °C, which is attributed to the reduction of NiO interacting with Al₂O₃–MgO support. The last peak generally exists at a temperature higher than 600 °C, since the peak is caused by the reduction of Ni²⁺ in the spinel phase, the form of strong metal–support interaction. However, there is tendency for an increase in the reducibility of nickel in the 10NAM catalyst (Figures 7 and 10). It is possibly due to some interaction between NiO and PU or PVA support; thus, H₂-TPR at a higher temperature and using CuO as a standard for TPR to determine the amount of H₂ should be studied in future work.

Figure 11 demonstrates three zones of hydrogen desorption of the H₂-TPD profile of the 100CF-10NAM ceramic foam

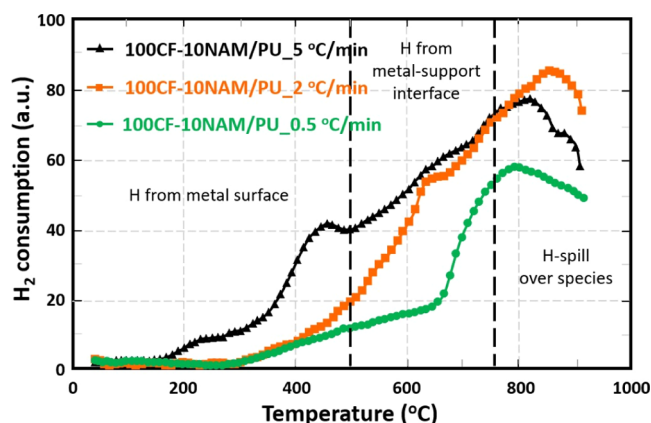


Figure 11. H₂-TPD of ceramic foam catalysts with different decomposition rates.

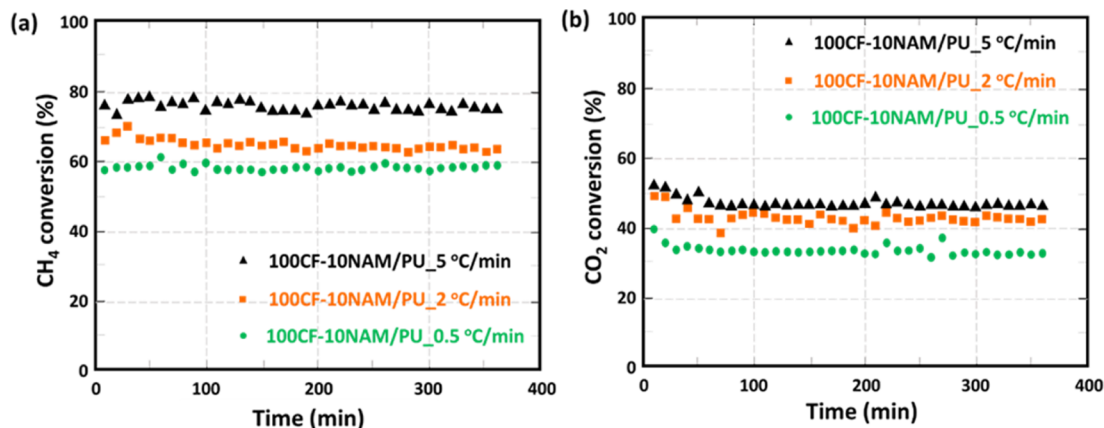
catalyst with different decomposition rates. The H₂-desorption below 450 °C was attributed to the H₂ adsorption on metal Ni sites, while the H₂ desorption between 450 and 750 °C

Table 6. Characterizations of Ceramic Foam Catalysts Related to Decomposition Rates of PU Foam Templates

catalyst	surface area (m ² /g)	pore volume (cm ³ /g)	average pore size (nm)	metal oxide dispersion (%)
100CF-10NAM/PU _{0.5} °C/min	51.00	0.20	15.76	3.28
100CF-10NAM/PU _{2.0} °C/min	53.00	0.22	16.92	4.67
100CF-10NAM/PU _{5.0} °C/min	65.00	0.21	18.97	7.44

Table 7. Catalytic Activity of the DRM (Operating Conditions: $T = 620\text{ }^{\circ}\text{C}$, $P = 1\text{ atm}$, and Total Flow 60 mL/min)

catalyst	% conversion		% yield		% selectivity		H_2/CO ratio
	CH_4	CO_2	H_2	CO	H_2	CO	
100CF-10NAM/PU_0.5 $^{\circ}\text{C/min}$	56.46	32.30	42.97	85.00	32.67	64.65	0.51
100CF-10NAM/PU_2 $^{\circ}\text{C/min}$	63.11	41.38	72.72	113.50	38.11	59.46	0.64
100CF-10NAM/PU_5 $^{\circ}\text{C/min}$	74.71	45.67	63.88	88.44	40.86	56.55	0.72

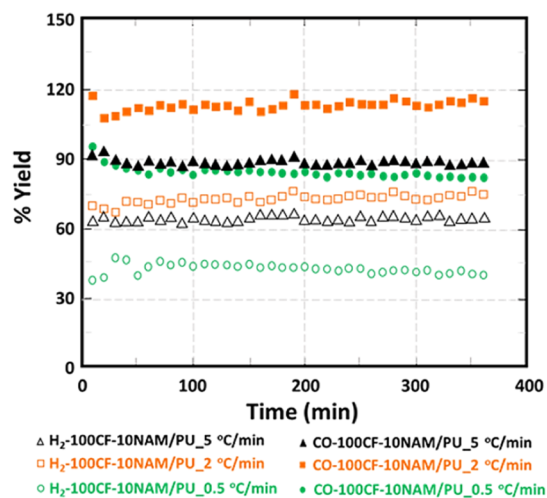
Figure 12. Catalytic activity of CH_4 conversion (a) and CO_2 conversion as a function of time (b).

described about the H_2 from the metal–support interface. The temperature higher than $750\text{ }^{\circ}\text{C}$ was related to H_2 spillover species.⁴⁶ In the first region, 100CF-10NAM/PU_5 $^{\circ}\text{C/min}$ provided the best H_2 adsorption on Ni active sites, whereas the 100CF-10NAM/PU_2 $^{\circ}\text{C/min}$ was as effective as the 100CF-10NAM/PU_5 $^{\circ}\text{C/min}$ in terms of H_2 consumption related to a metal–support interface. The 100CF-10NAM/PU_2.0 $^{\circ}\text{C/min}$ seemed to have more impact on hydrogen spillover as indicated in the last region. The hydrogen spillover is a phenomenon investigated characteristically at transition metal nanoparticle support interfaces and is a well-recognized phenomenon defined as the transport of adsorbed dissociated hydrogen from one surface to another by surface diffusion.⁶⁸ From the experimental results in this part, it can be concluded that the reducing temperature of $620\text{ }^{\circ}\text{C}$ is a benchmark for the operating temperature of further performance tests in dry reforming reaction. The various heating rates for foam removal were observed with regard to reaction performance as well.

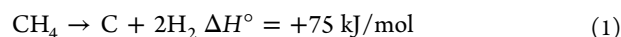
Catalytic Performance Test. The authors would like to explain a conceptual idea to select CF-10NAM for this research before criticizing the experimental results concerning the reaction efficiency. Nickel (Ni) is an attractive metal because it is economical compared to noble metals, and it is efficient in catalysis in the methane gas conversion process, with high reactivity and selectivity.⁶⁹ The selection of a catalyst support is imperative for the reaction that occurs between a metal surface and a catalyst support. The prevailing catalyst supports are metal oxides with high surface areas such as silica (SiO_2), alumina (Al_2O_3), zeolites, and so forth. Al_2O_3 and SiO_2 types are preferred in industry, especially for their use as the nickel metal support in methane-reforming processes.⁷⁰ CF-10NAM is an abbreviation for 10 % wt of nickel oxide on ceramic foam made from alumina magnesium support. This formulation was previously developed and studied by our research group.⁶⁴ According to the experimental activities, the catalytic activity of 100CF-10NAM ceramic foam catalysts for DRM (CH_4) at 620

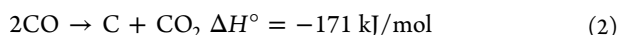
$^{\circ}\text{C}$ under atmospheric pressure was investigated and the results were summarized in Table 7.

All catalysts can maintain stable CH_4 conversion after 50 min, the 100CF-10NAM/PU_5 $^{\circ}\text{C/min}$ catalyst provided the highest CH_4 consumption followed by 100CF-10NAM/PU_2 $^{\circ}\text{C/min}$ and 100CF-10NAM/PU_0.5 $^{\circ}\text{C/min}$, in which the conversions were 74, 63, and 56%, respectively (Figure 12). The H_2 and CO yields of those created catalysts are displayed in Figure 13. The H_2 percentage yields of 100CF-10NAM/PU_2.0

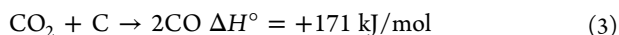
Figure 13. % H_2 and % CO yields of DRM over the 100CF-10NAM catalyst with decomposition rates of 0.5, 2, and $5\text{ }^{\circ}\text{C/min}$.

$^{\circ}\text{C/min}$ were considerably higher than the theoretical value that may be caused by side reactions producing hydrogen and carbon dioxide, for example, the decomposition of CH_4 and disproportionation of CO , as shown in eqs 1 and 2, respectively.^{71–73}





The decomposition of methane occurred at reaction temperatures above 553 °C, while at the reaction temperature below 674 °C, occurred the Boudouard reaction. Consequently, coke deposition would promptly generate temperatures in the range of 553–674 °C, as shown in eqs 3 and 4, respectively.^{74–76}



CONCLUSIONS

The technique of converting industrial foam scrap into a value-added product as a catalyst template for ceramic foam support production is demonstrated in this study. This project is a case study to see if it is possible to make a ceramic foam catalyst for the DRM reaction. A replication method was used to successfully prepare the 10NAM ceramic foam catalyst by utilizing a PU foam template. The following are the key findings of this study: with its linked open-cell architecture and fluid absorption ability, PU foam was an attractive candidate for the template. A sol–gel approach was used to generate the catalyst fluid or slurry, and the slurry viscosity had a substantial impact on ceramic foam parameters such as density, cell structure strength, Ni catalyst dispersion, and catalyst surface area. The best 10NAM slurry was made with 100CF-10NAM and no dilution. It had the best Ni dispersion and surface area of any of the catalysts. The rate of polymer decomposition in relation to the rate of heating during the decomposition stage is critical for cell-structure shaping. The correct rate of heating was 5 °C/min. The temperature for hydrogen reduction was obtained by investigating the catalyst properties during the reaction. The optimum temperature for the DRM reaction was 620 °C, which was imposed. The issue that is a necessity to pay attention to the development of our future work is the reducibility of nickel in the 10NAM catalyst at a temperature higher than 850 °C to investigate the effect of interaction between the polymer template and the catalyst. The metal oxide dispersion on ceramic foam materials dominates the activity of ceramic foam catalysts for DRM. The best catalytic performance was associated with a heating rate of 5.0 °C/min and a metal dispersion of 7.44%. 74% CH₄ conversion, 46% CO₂ conversion, 64% H₂ yield, 88% CO yield, and 0.72 H₂/CO ratio were the best results for driving the DRM reaction (Figures 14 and 15). However, by optimizing an operating state, the response performance can be improved and side reactions can be avoided. To develop ceramic foam, diverse foam features from various types of industrial PU wastes are being investigated.

EXPERIMENTAL METHODOLOGY

Polymeric Foam Selection and Characterization. Four types of polymer foams: PU, PVA, EPE, and EPP, from furniture and packaging factories in Bangkok were used as a template. They were cut into a geometric size of 25 × 25 × 25 mm for the determination of the cell content by the gas pycnometer technique under 3 psig of atmospheric pressure and 23 °C of system temperature according to ASTM D6226. The surface morphology and microstructure of the surplus foams were observed via scanning electron microscope (JSM 7600 F, JEOL) and OM (BH2-UMA, Olympus). Microscopic images were interpreted via analysis software (SemAfore 5.21) for determining the cell size, cell density, and strut size. Twenty specimens of

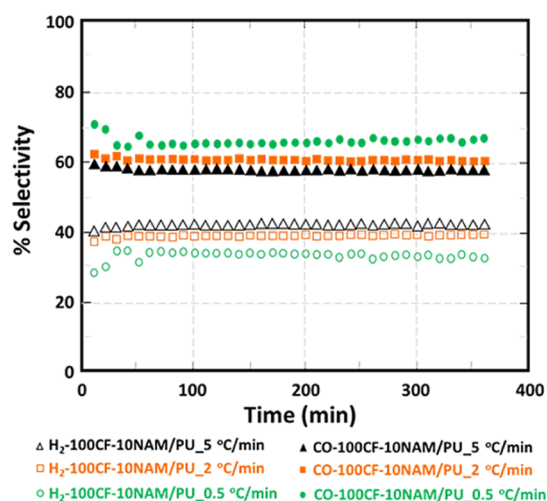


Figure 14. % H₂ and % CO selectivity of DRM over the 100CF-10NAM catalyst with decomposition rates of 0.5, 2, and 5 °C/min.

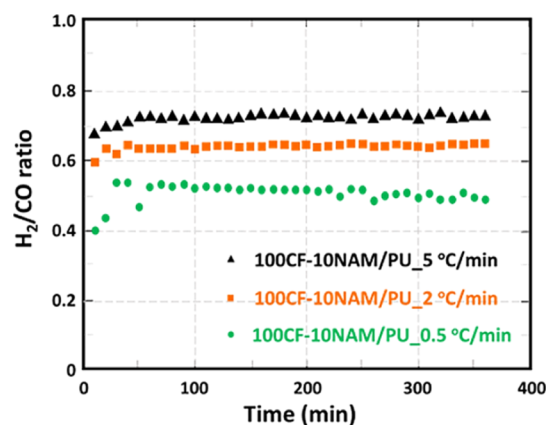


Figure 15. H₂/CO ratio of DRM over the 100CF-10NAM catalyst with decomposition rates of 0.5, 2, and 5 °C/min.

each sample were cut into a geometric size of 10 × 10 × 10 mm to determine those values from OM images. The thermal degradation behavior of polymeric foams was studied using TGA (TGA/DSC1, Mettler Toledo) to impose an operating condition for the thermal treatment and sintering process. The operating condition was controlled at 30–800 °C of the testing temperature and 5 °C/min of the heating rate according to ASTM E1131-03.

Fabrication of the Ceramic Foam-Supported Catalyst.

The experimental activities of catalyst preparation can be separated into two main parts: catalyst slurry preparation and catalyst support formation. First of all, the Al₂O₃–MgO-supported nickel catalyst (10NAM) was prepared via the sol–gel method. 10.016 g of alumina isopropoxide [Al(OC₃H₇)₃; Acros Organics] and 25.00 mL of deionized water were mixed in a round-bottom flask, and the solution was mixed for 20 min to achieve well dissolution. The round-bottom flask was installed into a reflux condenser for continuous stirring at 85 °C for 1 h; note that the water circulating system was not operated during this period. At the end of 1 h, 10 mL of 1 M nitric acid (HNO₃; Carlo Erba) was added into the flask, and then the solution turned to give a milky slurry appearance. The reflux condensation of the slurry was consequently manipulated at 85 °C for 20 h. The aqueous solution containing 7.098 g of magnesium ethoxide (Mg(OC₂H₅)₂; Aldrich) and 27.00 mL of

deionized water was prepared by mixing this solution for 20 h to obtain homogeneity; the solution gradually turned cloudy brown. $\text{Mg}(\text{OC}_2\text{H}_5)_2$ solution was then added into a reflux condenser for the condensation that had been run for 20 h; this process yielded a light brown, viscous slurry. Next, 25.00 mL of deionized water was added, and the reflux condensation was continued for 2 h. The final slurry was cooled down to room temperature, and 2.50 mL of nickel(II) nitrate hexahydrate ($\text{Ni}(\text{NO}_3)_2 \cdot 6\text{H}_2\text{O}$; QRëCMTM) was introduced into the slurry. When the slurry became light green, 50.00 mL of deionized water was added for 1 h mixing. The foam templates with a geometric size of 20.0 mm x 20.0 mm x 20.0 mm were cut for the 10NAM slurry coating. The templates were completely immersed in ceramic slurry and freed from the excess slurry by manual squeezing. The squeezed foams were aged at room temperature for 48 h before they were dried in an oven at 80 °C for 24 h; afterward, the polymer foams were calcined by sintering at temperatures above 1000 °C in air. The polymer templates decomposed during the calcination, whereas the ceramic particles were sintering. Finally, the ceramic foam structure replaced the polymer foam scaffold.

Rheological Measurements. As previously stated, the flow behavior of the manufactured catalyst slurry has a direct impact on coating performance; thus, the rheological behavior of catalyst slurries containing various concentrations of formulated 10NAM catalysts (Table 8) was examined using a rotational

Table 8. Composition of Ceramic Slurry with Different Water Content^a

sample ID	composition (% v/v) 10NAM (%)
100CF-10NAM	100
75CF-10NAM	75
50CF-10NAM	50
25CF-10NAM	25

^aNote: 10NAM = 10 wt % Ni/Al₂O₃-MgO.

viscometer (Brookfield programmable V-II). The active metal distribution on the catalyst support and the absorption ability of the foam templates was linked to the viscosity tendency.

Characterizations of Ceramic Foam Catalysts. The characteristics and properties of created catalysts were validated to ensure reliability for a ceramic foam application. The morphology and geometric characteristics of 10NAM ceramic foam were observed using a scanning electron microscope (JSM 7600 F, JEOL), while the specific surface area of ceramic foam catalysts was measured by the BET technique (BELSORP mini-II, BEL) via nitrogen adsorption at -196 °C. For the measurement through BET, the pelletized catalysts (0.2 g) were sieved to control their sizes in the range of 355–710 μm; they were consequently filled into a sample cell prior to surface conditioning and moisture removal under a nitrogen atmosphere at 350 °C for at least 4 h before the test was started. The reducibility of ceramic foam catalysts was investigated by H₂-TPR. 0.2 g of the catalyst sample was placed in a fixed-bed catalytic reactor (1/4" stainless-steel tube), whereupon the catalyst surface conditioning was carried out at 220 °C with a heating rate of 10 °C/min for 30 min; this pretreatment was manipulated under an argon (Ar) atmosphere with a 30 mL/min flow rate. The sample was heated in reduced gas (5% of H₂/Ar) under a flow rate of 30 mL/min in the temperature range of 40 to 900 °C with a heating rate of 10 °C/min. The hydrogen consumption was monitored using a thermal conductivity

detector [gas chromatography (GC) model 6820, Agilent]. The metal dispersion of ceramic foam catalysts was characterized using temperature-programmed desorption of hydrogen (H₂-TPD). The catalyst sample was pre-reduced in 30 mL/min of hydrogen (H₂) atmosphere at 700 °C for 4 h with a heating rate of 1 °C/min, and then it was cooled down to 100 °C with Ar flow at a heating rate of 10 °C/min for 30 min. Hydrogen desorption was carried out in the temperature range of 40–900 °C with Ar flow at a heating rate of 10 °C/min.

Catalytic Performance Test. A fixed-bed stainless-steel reactor was used to test the effectiveness of a 10NAM ceramic foam catalyst for DRM. Before the reaction, the catalyst was pre-treated for 30 min at ambient temperature with a N₂ stream to eliminate additional impurities and then reduced for 20 h with a 30 mL/min H₂ flow at 620 °C. The gaseous mixture was permitted to pass through the catalyst bed at a total flow of 60 mL/min (CH₄/CO₂/N₂ = 15:25:20 mL/min) until the temperature in the reactor reached 620 °C with a heating rate of 7 °C/min at atmospheric pressure. On-line GC (model 6890 N, Agilent) with TCD detectors was used to determine the product compositions. Helium (He) was used as the carrier gas. Figure 16 illustrates the setup for the DRM experiment. The bed

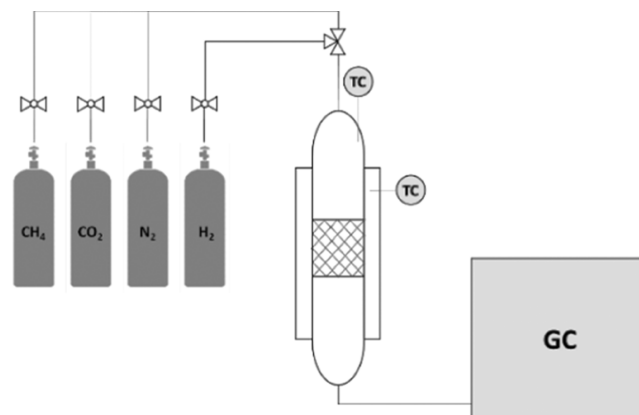


Figure 16. Schematic diagram of the DRM process.

was at a total flow of 60 mL/min (CH₄/CO₂/N₂ = 15:25:20 mL/min) until the temperature in the reactor reached 620 °C with a heating rate of 7 °C/min at atmospheric pressure.

AUTHOR INFORMATION

Corresponding Author

Rungsima Yeetsorn – *The Sirindhorn International Thai-German Graduate School of Engineering, King Mongkut's University of Technology North Bangkok, Bangkok 10800, Thailand*; orcid.org/0000-0002-8029-0305; Phone: +66 2555 2000 ext. 1504; Email: rungsima.y@tggs.kmutnb.ac.th

Authors

Sabaithip Tungkamani – *Research and Development Center for Chemical Engineering Unit Operation and Catalyst Design (RCC), King Mongkut's University of Technology North Bangkok, Bangkok 10800, Thailand*

Yaowaret Maiket – *Thai-French Innovation Institute, King Mongkut's University of Technology North Bangkok, Bangkok 10800, Thailand*

Complete contact information is available at:
<https://pubs.acs.org/10.1021/acsomega.1c05841>

Notes

The authors declare no competing financial interest.

ACKNOWLEDGMENTS

The authors gratefully acknowledge financial support from the National Science Research and Innovation Fund (NSRF) (grant no. KMUTNB-BasicR-64-28-1) and PTT Public Company Limited. We also would like to express our appreciation for research assistance from Anucha Sangsuriyan.

REFERENCES

- (1) Wichai-utcha, N.; Chavalparit, O. 3Rs Policy and plastic waste management in Thailand. *J. Mater. Cycles Waste Manag.* **2018**, *21*, 10–22.
- (2) McCue, A.; Elizalde, B.; Kometsofpa, P.; Cui, M. B.; Gillies, P. M. *Scaling Up Circular Strategies to Achieve Zero Plastic Waste in Thailand*; Gland: World Wide Fund for Nature, 2020.
- (3) Jin, F.-L.; Zhao, M.; Park, M.; Park, S.-J. Recent trends of foaming in polymer processing: A review. *Polymers* **2019**, *11*, 953.
- (4) Twigg, M. V.; Richardson, J. T. Theory and applications of ceramic foam catalysts. *Trans. Inst. Chem. Eng.* **2002**, *80*, 183–189.
- (5) Richardson, J. T.; Remue, D.; Hung, J.-K. Properties of ceramic foam catalyst supports: mass and heat transfer. *Appl. Catal., A* **2003**, *250*, 319–329.
- (6) Cordier, A.; Rossignol, F.; Laurent, C.; Chartier, T.; Peigney, A. A new fast method for ceramic foam impregnation: Application to the CCVD synthesis of carbon nanotubes. *Appl. Catal., A* **2007**, *319*, 7–13.
- (7) Nor, M. A. A. M.; Hong, L. C.; Ahmad, Z. A.; Md Akil, H. Preparation and characterization of ceramic foam produced via polymeric foam replication method. *J. Mater. Process. Technol.* **2008**, *207*, 235–239.
- (8) Faure, R.; Rossignol, F.; Chartier, T.; Bonhomme, C.; Maitre, A.; Etchegoyen, G.; Del Gallo, P.; Gary, D. Alumina foam catalyst supports for industrial steam reforming processes. *J. Eur. Ceram. Soc.* **2011**, *31*, 303–312.
- (9) Calati, M.; De Monte, E.; Mancin, S. Numerical Analysis of the Effects of the Structure Shape and Orientation of Kelvin Cell Porous Structures during Air Forced Convection. *Appl. Sci.* **2021**, *11*, 6189.
- (10) Ghoneim, S. A.; El-Salamony, R. A.; El-Temtamy, S. A. Review on innovative catalytic reforming of natural gas to syngas. *World J. Eng. Technol.* **2016**, *04*, 116.
- (11) Carty, W. M.; Lednor, P. W. Monolithic ceramics and heterogeneous catalysts: honeycombs and foams. *Curr. Opin. Solid State Mater. Sci.* **1996**, *1*, 88–95.
- (12) Allison, C. B. The effects of turbulence structures on the air-side performance of compact tube-fin heat exchangers, Doctoral Dissertation, Adelaide Research & Scholarship, 2006.
- (13) Nor, M. A. A. M.; Hong, L. C.; Ahmad, Z. A.; Akil, H. M. Preparation and characterization of ceramic foam produced via polymeric foam replication method. *J. Mater. Process. Technol.* **2008**, *207*, 235–239.
- (14) Ahmad, S.; Latif, M. A.; Taib, H.; Ismail, A. F. Short review: Ceramic foam fabrication techniques for wastewater treatment application. *Adv. Mater.* **2013**, *795*, 5–8.
- (15) Mao, X. Processing of ceramic foams. Recent Advances in Porous Ceramics *IntechOpen*. **2018**, *31*, 47. DOI: 10.5772/intechopen.71006
- (16) Wang, M.; Xu, S. Preparation and applications of foam ceramics. *Earth Environ. Sci.* **2018**, *186*, 012066.
- (17) Owens, G. J.; Singh, R. K.; Foroutan, F.; Alqaysi, M.; Han, C.-M.; Mahapatra, C.; Kim, H.-W.; Knowles, J. C. Sol–gel based materials for biomedical applications. *Prog. Mater. Sci.* **2016**, *77*, 1–79.
- (18) Esposito, S. Traditional sol-gel chemistry as a powerful tool for the preparation of supported metal and metal oxide catalysts. *Materials* **2019**, *12*, 668.
- (19) Drioli, E.; Giorno, L. *Basic Aspects of Membrane Science and Engineering*; Science Press, 2012.
- (20) Chen, Y.; Wang, N.; Ola, O.; Xia, Y.; Zhu, Y. Porous ceramics: Light in weight but heavy in energy and environment technologies. *Mater. Sci. Eng. R Rep* **2021**, *143*, 100589.
- (21) Twigg, M. V.; Richardson, J. T. Fundamentals and applications of structured ceramic foam catalysts. *Ind. Eng. Chem. Res.* **2007**, *46*, 4166–4177.
- (22) Ambrosio, G.; Bianco, N.; Chiu, W. K. S.; Iasiello, M.; Naso, V.; Oliviero, M. The effect of open-cell metal foams strut shape on convection heat transfer and pressure drop. *Appl. Therm. Eng.* **2016**, *103*, 333–343.
- (23) Ahmad, H.; Saeid, B.; Rahmatolah, E.; Shirin, N. Different pore size alumina foams and study of their physical and mechanical properties. *Ceram.-Silik.* **2015**, *59*, 6–9.
- (24) Faure, R.; Rossignol, F.; Chartier, T.; Bonhomme, C.; Maitre, A.; Etchegoyen, G.; Gary, D. Alumina foam catalyst supports for industrial steam reforming processes. *J. Eur. Ceram. Soc.* **2001**, *31*, 303–312.
- (25) Krämer, R.; Zammarano, M.; Linteris, G. T.; Gedde, U.; Gilman, J. Heat release and structural collapse of flexible polyurethane foam. *Polym. Degrad. Stab.* **2010**, *95*, 1115–1122.
- (26) Hakim, A. A.; Nassar, M.; Emam, A.; Sultan, M. Preparation and characterization of rigid polyurethane foam prepared from sugar-cane bagasse polyol. *Mater. Chem. Phys.* **2011**, *129*, 301–307.
- (27) Gu, R.; Sain, M. M. Effects of wood fiber and microclay on the performance of soy based polyurethane foams. *J. Polym. Environ.* **2013**, *21*, 30–38.
- (28) Es-saheb, M.; Elzatahry, A. Post-heat treatment and mechanical assessment of polyvinyl alcohol nanofiber sheet fabricated by electrospinning technique. *Int. J. Polym. Sci.* **2014**, *2014*, 1–6. DOI: 10.1155/2014/605938
- (29) Pique, T. M.; Pérez, C. J.; Alvarez, V. A.; Vázquez, A. Water soluble nanocomposite films based on poly(vinyl alcohol) and chemically modified montmorillonite. *J. Compos. Mater.* **2014**, *48*, 545–553.
- (30) Ghalia, M. A.; Dahman, Y. Radiation crosslinking polymerization of poly (vinyl alcohol) and poly (ethylene glycol) with controlled drug release. *J. Polym. Res.* **2015**, *22*, 218–226.
- (31) Kang, X.; Kuga, S.; Wang, C.; Zhao, Y.; Wu, M.; Huang, Y. Green preparation of cellulose nanocrystal and its application. *ACS Sustain. Chem. Eng.* **2018**, *6*, 2954–2960.
- (32) Nor, M. A. A. M.; Hong, L. C.; Ahmad, Z. A.; Akil, H. M. Preparation and characterization of ceramic foam produced via polymeric foam replication method. *J. Mater. Process. Technol.* **2008**, *207*, 235–239.
- (33) Cychosz, K. A.; Thommes, M. Progress in the physisorption characterization of nanoporous gas storage materials. *Engineering* **2018**, *4*, 559–566.
- (34) Guerra-Que, Z.; Pérez-Vidal, H.; Torres-Torres, G.; Arévalo-Pérez, J. C.; Pavón, A. A. S.; Cervantes-Urbe, A.; de los Monteros, A. E.; Lunagómez-Rocha, M. A. Treatment of phenol by catalytic wet air oxidation: a comparative study of copper and nickel supported on γ -alumina, ceria and γ -alumina–ceria. *RSC Adv.* **2019**, *9*, 8463–8479.
- (35) Alothman, Z. A review: Fundamental aspects of silicate mesoporous. *Materials* **2012**, *5*, 2874–2902.
- (36) Yurdakal, S.; Garlisi, C.; Özcan, L.; Bellardita, M.; Palmisano, G. (Photo) catalyst characterization techniques: adsorption isotherms and BET, SEM, FTIR, UV–Vis, photoluminescence, and electrochemical characterizations. *Heterog. Photocatal.* **2019**, *1*, 87–152.
- (37) Hurst, N. W.; Gentry, S. J.; Jones, A.; McNicol, B. D. Temperature programmed reduction. *Catal. Rev.—Sci. Eng.* **1982**, *24*, 233–309.
- (38) Liu, H.; Da Costa, P.; Taief, H. B. H.; Benzina, M.; Gálvez, M. E. Mg-promotion of Ni natural clay-supported catalysts for dry reforming of methane. *RSC Adv.* **2018**, *8*, 19627–19634.
- (39) Znak, L.; Jerzy, Z. Effects of support on hydrogen adsorption/desorption on nickel. *Appl. Catal. Gen.* **2008**, *334*, 268–276.
- (40) Villa, R.; Cinzia, C.; Gianpiero, G.; Luca, L.; Pio, F.; Ugo, C.; Stefano, R. Ni based mixed oxide materials for CH₄ oxidation under redox cycle conditions. *J. Mol. Catal. A: Chem.* **2003**, *204–205*, 637–646.

- (41) Ciambelli, P.; Palma, V.; Palo, E. Comparison of ceramic honeycomb monolith and foam as Ni catalyst carrier for methane autothermal reforming. *Catal* **2010**, *155*, 92–100.
- (42) Liu, J.; Li, C.; Wang, F.; He, S.; Chen, H.; Zhao, Y.; Wei, M.; Evans, D. G.; Duan, X. Enhanced low-temperature activity of CO₂ methanation over highly-dispersed Ni/TiO₂ catalyst. *Catal. Sci. Technol.* **2013**, *3*, 2627–2633.
- (43) Liu, Q.; Gao, J.; Zhang, M.; Li, H.; Gu, F.; Xu, G.; Zhong, Z.; Su, F. Highly active and stable Ni/ γ -Al₂O₃ catalysts selectively deposited with CeO₂ for CO methanation. *RSC Adv.* **2014**, *4*, 16094–16103.
- (44) Smeds, S.; Salmi, T.; Lindfors, L. P.; Krause, O. Chemisorption and TPD studies of hydrogen on Ni/Al₂O₃. *Appl. Catal. Gen.* **1996**, *144*, 177–194.
- (45) Ewald, S.; Standl, S.; Hinrichsen, O. Characterization of nickel catalysts with transient methods. *Appl. Catal. Gen.* **2018**, *549*, 93–101.
- (46) Infantes-Molina, A.; Gralberg, E.; Cecilia, J. A.; Finocchio, E.; Rodríguez-Castellón, E. Nickel and cobalt phosphides as effective catalysts for oxygen removal of dibenzofuran: role of contact time, hydrogen pressure and hydrogen/feed molar ratio. *Catal. Sci. Technol.* **2015**, *5*, 3403–3415.
- (47) Santos, D. C. R. M.; Lisboa, J. S.; Passos, F. B.; Noronha, F. B. Characterization of steam-reforming catalysts. *Braz. J. Chem. Eng.* **2004**, *21*, 203–209.
- (48) Zhang, H.; Dong, Y.; Fang, W.; Lian, Y. Effects of composite oxide supports on catalytic performance of Ni-based catalysts for CO methanation. *Chin. J. Catal.* **2013**, *34*, 330–335.
- (49) Nguyen, L. Q.; Abella, L. C.; Gallardo, S. M.; Hinode, H. Effect of nickel loading on the activity of Ni/ZrO₂ for methane steam reforming at low temperature. *React. Kinet. Catal. Lett.* **2018**, *93*, 227–232.
- (50) Zhu, X.; Jiang, D.; Tan, S. The control of slurry rheology in the processing of reticulated porous ceramics. *Mater. Res. Bull.* **2002**, *37*, 541–553.
- (51) Jiang, D. L.; Zhu, X. W. Preparation and properties of silicon carbide reticulated porous ceramics. *Key Eng. Mater.* **2003**, *247*, 19–26.
- (52) Ohji, T.; Fukushima, M. Macro-porous ceramics: processing and properties. *Key Eng. Mater.* **2012**, *57*, 115–131.
- (53) Voigt, C.; Aneziris, C. G.; Hubálková, J. Rheological characterization of slurries for the preparation of alumina foams via replica technique. *J. Am. Ceram. Soc.* **2015**, *98*, 1460–1463.
- (54) Mao, X. Processing of ceramic foams. *IntechOpen* **2018**, *1*, 31–47.
- (55) Gómez, S. Y.; Alvarez, O. A.; Escobar, J. A.; Neto, J. B. R.; Rambo, C. R.; Hotza, D. Relationship between rheological behavior and final structure of Al₂O₃ and YSZ foams produced by replica. *Adv. Mater. Sci. Eng.* **2012**, *2012*, 1–9.
- (56) Wojcieszak, R.; Jasik, A.; Monteverdi, S.; Ziolk, M.; Bettahar, M. M. Nickel niobia interaction in non-classical Ni/Nb₂O₅ catalysts. *J. Mol. Catal. Chem.* **2006**, *256*, 225–233.
- (57) Chettibi, S.; Benguedouar, Y.; Keghouche, N. The metal-support interaction in the oxide supported nickel nanoparticles synthesized by radiolysis. *Phys. Procedia* **2009**, *2*, 707–712.
- (58) Millet, M.-M.; Tarasov, A. V.; Girsdiess, F.; Algara-Siller, G.; Schlögl, R.; Frei, E. Highly Dispersed NiO/NixMg1-xO catalysts derived from solid solutions: how metal and support control the CO₂ hydrogenation. *ACS Catal.* **2019**, *9*, 8534–8546.
- (59) Abu-Jdayil, B.; Al-Nakoua, M. A.; El-Naas, M. H.; Khaleel, A. Rheological characteristics of nickel alumina sol-gel catalyst. *Fuel Process. Technol.* **2012**, *102*, 85–89.
- (60) Zhu, X.; Jiang, D.; Tan, S. The control of slurry rheology in the processing of reticulated porous ceramics. *Mater. Res. Bull.* **2002**, *37*, 541–553.
- (61) Velu, S.; Gangwal, S. Synthesis of alumina supported nickel nanoparticle catalysts and evaluation. *Solid State Ionics* **2006**, *177*, 803–811.
- (62) Yang, W.; Feng, Y.; Chu, W. Promotion effect of CaO modification on mesoporous Al₂O₃-supported Ni catalysts for CO₂ methanation. *Int. J. Chem. Eng.* **2016**, *2016*, 1–7.
- (63) Fujii, T.; Messing, G. L.; Huebner, W. Processing and Properties of Cellular Silica Synthesized by Foaming Sol-Gels. *J. Am. Ceram. Soc.* **1990**, *73*, 85–90.
- (64) Phongaksorn, M.; Tungkamani, S.; Dharmasaroja, N.; Sornchamni, T.; Chuvaree, R.; Kanjanabat, N.; Siri-Nguan, N. Elucidation of the influence of Ni-Co catalytic properties on dry methane reforming performance. *Chem. Eng. Trans.* **2015**, *43*, 925–930.
- (65) Piyapaka, K.; Tungkamani, S.; Phongaksorn, M. Effect of strong metal support interactions of supported Ni and Ni-Co catalyst on metal dispersion and catalytic activity toward dry methane reforming reaction. *Appl. Sci. Eng. Prog.* **2016**, *9*, 255–259.
- (66) Dharmasaroja, N.; Ratana, T.; Tungkamani, S.; Sornchamni, T.; Simakov, D. S. A.; Phongaksorn, M. The Effects of CeO₂ and Co Doping on the Properties and the Performance of the Ni/Al₂O₃-MgO Catalyst for the Combined Steam and CO₂ Reforming of Methane Using Ultra-Low Steam to Carbon Ratio. *Catalysts* **2020**, *10*, 1450.
- (67) Jin, B.; Li, S.; Liang, X. Enhanced activity and stability of MgO-promoted Ni/Al₂O₃ catalyst for dry reforming of methane: Role of MgO. *Fuel* **2021**, *284*, 119–082.
- (68) Mukherjee, S.; Ramalingam, B.; Gangopadhyay, S. Hydrogen spillover at sub-2 nm Pt nanoparticles by electrochemical hydrogen loading. *J. Mater. Chem. A* **2014**, *2*, 3954–3960.
- (69) Chen, L.; Qi, Z.; Zhang, S.; Su, J.; Somorjai, G. A. Catalytic hydrogen production from methane: A review on recent progress and prospect. *Catalysts* **2020**, *10*, 858.
- (70) Shinde, P. S.; Suryawanshi, P. S.; Patil, K. K.; Belekar, V. M.; Sankpal, S. A.; Delekar, S. D.; Jadhav, S. A. A Brief Overview of Recent Progress in Porous Silica as Catalyst Supports. *J. Compos. Sci.* **2021**, *5*, 75.
- (71) Sangsuriyan, A.; Yeetsorn, R.; Tungkamani, S.; Sornchamni, T. Polymeric Material Application for The Production of Ceramic Foam Catalyst. *Int. J. Appl. Ceram. Technol.* **2015**, *3*, 21–30.
- (72) Srisurat, T.; Pana-Suppamassadu, K.; Narataruksa, P.; Tungkamani, S.; Phongaksorn, M.; Sornchamni, T. Syngas production via carbon dioxide reforming of methane in a wall-coated monolith reactor. *Adv. Mater. Res.* **2013**, *805–806*, 1257–1264.
- (73) Singh, R.; Dhir, A.; Mohapatra, S. K.; Mahla, S. K. Dry reforming of methane using various catalysts in the process: review. *Biomass Convers. Biorefin.* **2020**, *10*, 567–587.
- (74) Shamsi, A.; Johnson, C. D. Effect of pressure on the carbon deposition route in CO₂ reforming of CH₄. *Catal* **2003**, *84*, 17–25.
- (75) Arora, S.; Prasad, R. An overview on dry reforming of methane: strategies to reduce carbonaceous deactivation of catalysts. *RSC Adv.* **2016**, *6*, 108668–108688.
- (76) Gao, Y.; Jiang, J.; Meng, Y.; Yan, F.; Aihemaiti, A. A review of recent developments in hydrogen production via biogas dry reforming. *Energy Convers. Manag.* **2018**, *171*, 133–155.